

Deep Stereo Image Compression with Decoder Side Information using Wyner Common Information

Nitish Mital^{1,†}, Ezgi Özyılkan^{1,†}, Ali Garjani^{1,‡}, and Deniz Gündüz[†]

[†]*Department of Electrical and Electronics Engineering, Imperial College London*

[‡]*Department of Computer Engineering, Sharif University of Technology*
 {n.mital, ezgi.ozyilkan17,d.gunduz}@imperial.ac.uk, garjania@ce.sharif.edu

Abstract

We present a novel deep neural network (DNN) architecture for compressing an image when a correlated image is available as side information only at the decoder. This problem is known as distributed source coding (DSC) in information theory. In particular, we consider a pair of stereo images, which generally have high correlation with each other due to overlapping fields of view, and assume that one image of the pair is to be compressed and transmitted, while the other image is available only at the decoder. In the proposed architecture, the encoder maps the input image to a latent space, quantizes the latent representation, and compresses it using entropy coding. The decoder is trained to extract the Wyner’s common information between the input image and the correlated image from the latter. The received latent representation and the locally generated common information are passed through a decoder network to obtain an enhanced reconstruction of the input image. The common information provides a succinct representation of the relevant information at the receiver. We train and demonstrate the effectiveness of the proposed approach on the KITTI dataset of stereo image pairs. Our results show that the proposed architecture is capable of exploiting the decoder-only side information, and outperforms previous work on stereo image compression with decoder side information.

1 Introduction

Data compression is a fundamental and well-studied problem in engineering, and is commonly formulated with the goal of designing codes with minimal average code length for a given data ensemble. Shannon showed that the entropy is a fundamental bound in lossless data compression when multiple independent samples of the information source can be compressed jointly while allowing arbitrarily small probability of error. The design of entropy codes relies on modeling the probability distribution of the data ensemble. Continuous-valued data (such as vectors of image pixel intensities) must also be quantized to a finite set of discrete values, which introduces error. In this context, known as the lossy compression problem, one must trade off two competing costs: the entropy of the discretized representation (rate) and the error arising from the quantization (distortion). In the case of lossy compression, the fundamental performance bound is characterized by the information theoretic rate-distortion curve. Recently, deep neural network (DNN) aided data-driven image compression algorithms have received significant research interest, and achieved impressive performance results, outperforming classical methods, such as JPEG2000 (Skodras et al. [2001]) and BPG (Bellard).

¹Contributed equally to this work.

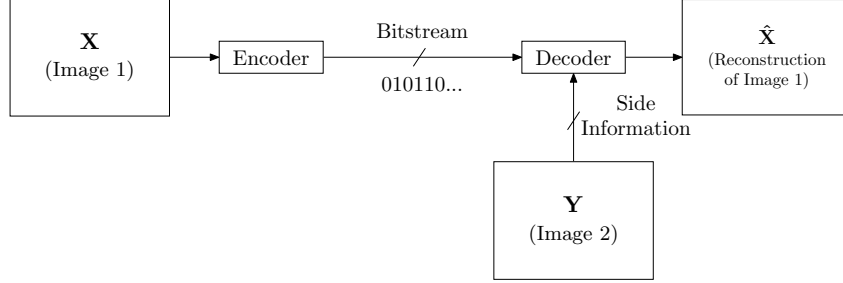


Figure 1: System model for lossy source compression with decoder-only side information.

In this work, we are interested in DNN-aided *distributed image compression*, where side information in the form of a correlated image is available only at the decoder. This scenario, illustrated in Fig. 1, occurs, for example, in the case of a pair of stereo cameras, where two cameras capture images of a scene from different angles at the same moment. In this case, the two images are highly correlated due to overlapping fields of view. The two cameras do not communicate with each other, and therefore, cannot apply joint encoding of the images as in Liu et al. [2019]. Assume that the left camera delivers its image (in a lossless fashion) to the destination, e.g., a central storage or processing unit. The right camera, instead of employing a standard image compression algorithm, should be able to benefit from the presence of a highly correlated image from the left camera, even though it does not have access to this image. Another application of the proposed setup is in video coding, where each frame is compressed individually (to transfer complexity from encoder to decoder) conditioned on the previous frames (Aaron et al. [2003]).

The benefit of decoder-only side information in compression goes back to Slepian and Wolf’s seminal work on distributed lossless compression (Slepian and Wolf [1973]). They showed that a compression rate equal to the entropy of the source conditioned on the side information is necessary and sufficient for lossless compression. Interestingly, the same rate is also necessary when the side information is available to both the encoder and the decoder. This was later extended by Wyner and Ziv to lossy compression with decoder side information in Wyner and Ziv [1976]. They showed that the decoder side information can provide unbounded gains in rate; however, there is a non-zero rate loss in general compared to having the side information both at the encoder and the decoder.

In this paper, we propose a novel neural architecture to perform lossy compression of an image assuming that its stereo pair is available at the decoder, which is used as side information. The novelty of the proposed method lies in employing the concept of Wyner common information to first learn the common features between the two correlated images. Wyner common information generated by the decoder is then used along with the quantized latent representation of the original image conveyed by the encoder to reconstruct the original image. We show that our proposed method achieves a significantly better rate-distortion trade-off at low bit rates than the state of the art single image compression algorithms, as well as similar previous works on deep stereo image compression with decoder side information (Ayzik and Avidan [2020]).

1.1 Related work

Deep image compression: There has been a surge of interest in DNN models for image compression, most notably Ballé et al. [2017], Ballé et al. [2018], Toderici et al. [2017], Theis et al. [2017], Minnen et al. [2018], Lee et al. [2019], Patel et al. [2021]. State of the art neural image compression models outperform traditional image compression codecs like JPEG2000 and BPG. In Ballé et al. [2017], a DNN-based image compression algorithm is proposed, where the linear transform code is replaced by a DNN, and the distribution of the quantized latent vector is learned from data for efficient entropy coding. An extension is proposed in Ballé et al. [2018] by introducing a hyperprior to capture the spatial dependencies between the elements of the latent representation by estimating their standard deviations, thus enabling better compression of the latent representation by the entropy coder. In Lee et al. [2019], the authors generalize the hyperpriors of Ballé et al. [2018] by estimating the means of the elements of the latent representations in addition to their standard deviations, and thus improve the compression performance. Note that the works mentioned enhance compression by generating more accurate estimations of the entropy model of the image. In Patel et al. [2021], the authors

introduce the concept of saliency-driven image compression, which compresses different areas of an image at different rates by modeling their saliency, thus providing better image reconstructions in terms of human perception than previous DNN-based approaches.

Deep image compression with side information: The work that is most related to ours is by Ayzik and Avidan [2020], in which the authors also consider the problem of distributed source coding with decoder side information. The method proposed in Ayzik and Avidan [2020] first reconstructs the image at the decoder using the autoencoder architecture of Mentzer et al. [2018], which is then refined with the help of the side information image. Their approach can be considered as post-processing of the image with side information.

We provide a different solution to the distributed source coding problem, which provides better performance as well as a solid theoretical foundation based on variational inference and information theory. Our method enhances compression by learning common features between the input image and the side information at the decoder, and using them for reconstruction, thus enabling the encoder to transmit only the information about the input image that is missing in the side information. We employ techniques used in previous works in the literature that, like us, use the Wyner common information to model dependent random variables (Wang et al. [2016], Ryu et al. [2020]), and generalize them to complex, non-parametric prior densities, that allows the DNN to learn on complex datasets.

2 Background

2.1 Wyner-Ziv compression

Wyner and Ziv showed in (Wyner and Ziv [1976]) that having correlated side information even only at the decoder can help reduce the rate in lossy compression. The Wyner-Ziv model, illustrated in Fig. 1, corresponds to the distributed source coding scenario we study in this paper. Let X and Y denote the source and side information variables, respectively, with joint distribution $p(x, y)$. Consider a distortion measure $D(\cdot, \cdot)$, where the average distortion between the input sequence $\mathbf{x} \in \mathbb{R}^n$ and its reconstruction $\hat{\mathbf{x}} \in \mathbb{R}^n$ is given by $\frac{1}{n} \sum_{i=1}^n D(x_i, \hat{x}_i)$. The information theoretic fundamental limit in lossy compression is characterized by the *rate-distortion function*, given by

$$R_{X|Y}^{WZ}(d) = \inf I(X; V | Y), \quad (1)$$

where $R^*(d)$ is the rate of compression (in bits per source sample) to achieve a given target average distortion d , and the infimum is with respect to all auxiliary random variables V and reconstruction functions $f : \mathcal{Y} \times \mathcal{V} \rightarrow \hat{\mathcal{X}}$ that satisfy: i) V and Y are conditionally independent given X , that is, $V - X - Y$ form a Markov chain; ii) $\mathbb{E}[D(X, f(V, Y))] \leq d$.

2.2 Wyner common information

We will employ the concept of *Wyner common information* (Wyner [1975]), which models the dependence between two random variables X and Y . It is defined as

$$C(X; Y) = \inf I(X, Y; W), \quad (2)$$

where the infimum is taken over all the auxiliary random variables W such that $X - W - Y$ form a Markov chain. Note that this implies that $p(w | x, y) = p(w | y)$.

2.3 Compression with variational models

In this section, we describe a variational model for single image compression, proposed in Ballé et al. [2017], that we use as our baseline. We choose this baseline because it is a light model that also provides a very good performance.

Let us denote the input image at the encoder by \mathbf{x} , and the correlated stereo image at the decoder by \mathbf{y} . In the *transform coding* approach (Goyal [2001]), the encoder transforms the input image vector $\mathbf{x} \in \mathbb{R}^n$ using a *parametric analysis transform*, denoted by the function \mathbf{g}_a , to a latent representation $\mathbf{v}_x = \mathbf{g}_a(\mathbf{x}; \phi_x) \in \mathbb{R}^m$, where ϕ_x refers to the parameters of the transform, e.g., weights of the corresponding DNN. The latent representation \mathbf{v}_x is quantized to $\hat{\mathbf{v}}_x \in \mathbb{Z}^m$. Since the quantization

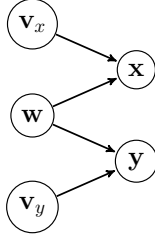


Figure 2: Graphical model. The Markov chains $\mathbf{v}_x - \mathbf{x} - \mathbf{y}$, $\mathbf{x} - \mathbf{w} - \mathbf{y}$ and $\mathbf{x} - \mathbf{y} - \mathbf{v}_y$ are also implied by this graphical model.

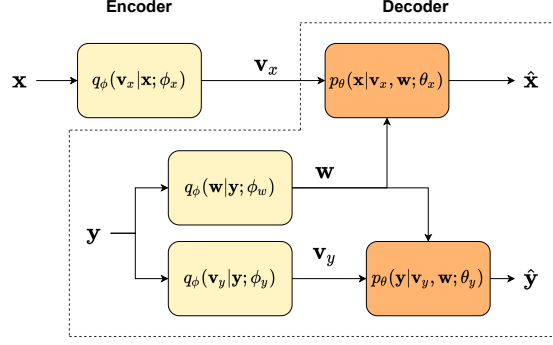


Figure 3: Distributed source coding architecture.

step is a non-differentiable operation, which prevents end-to-end training, it is instead replaced by additive uniform random noise over $[-0.5, 0.5]$ during training (Ballé et al. [2017]). Thus \mathbf{v}_x is perturbed by uniform noise during training to obtain $\tilde{\mathbf{v}}_x$, which approximates the quantized latents $\hat{\mathbf{v}}_x$. The “inference” mechanism, where the latent representation of the input image is computed and uniform noise is added to it, is modeled in Ballé et al. [2017] as follows:

$$q_\phi(\tilde{\mathbf{v}}_x | \mathbf{x}; \phi_x) = \prod_i \mathcal{U}\left(\tilde{v}_x(i) \mid v_x(i) - \frac{1}{2}, v_x(i) + \frac{1}{2}\right), \quad \text{with } \mathbf{v}_x = \mathbf{g}_a(\mathbf{x}; \phi_x), \quad (3)$$

where $\mathcal{U}(\cdot)$ denotes a uniform distribution on $v_x(i)$. The probability distribution of \mathbf{v}_x is modeled using a univariate non-parametric, fully factorized density function in Ballé et al. [2017]:

$$p(\tilde{\mathbf{v}}_x) = \prod_i \left(p_{v_x(i) | \psi^{(i)}}(\psi^{(i)}) * \mathcal{U}(-0.5, 0.5) \right)(\tilde{v}_x(i)), \quad (4)$$

where the vectors $\psi^{(i)}$ encapsulate the parameters of each univariate distribution $p_{v_x(i) | \psi^{(i)}}$.

During evaluation, the quantized latent representation $\tilde{\mathbf{v}}_x$ is encoded and transmitted as a bitstream by the arithmetic encoder using the univariate parametric density model. At the decoder, the bitstream corresponding to the latent representation is decoded by the arithmetic decoder, and mapped to the data space using a *synthesis* transform \mathbf{g}_s , which gives us $\hat{\mathbf{x}} = \mathbf{g}_s(\tilde{\mathbf{v}}_x; \theta_x)$, where θ_x refers to the weights of the neurons. Since the quantization step introduces error, we seek to achieve a reasonable performance trade-off between the reconstructed image quality and the compression rate. The loss function is defined as the weighted sum of the two objectives:

$$L(\mathbf{g}_a, \mathbf{g}_s) = R + \lambda D, \quad (5)$$

where D is the average distortion between the reconstructed and input images, and R is the rate of transmission, that is, the number of bits sent by the encoder. Minimizing this loss function for a given λ provides one point on the rate-distortion curve, while the whole curve can be obtained by varying λ .

3 Image compression using Wyner common information

In this section, we describe our main contribution, where we propose a novel autoencoder architecture for image compression exploiting the Wyner common information, \mathbf{w} , between the image to be reconstructed, \mathbf{x} , and the side information, \mathbf{y} . In the Wyner-Ziv characterization of the rate-distortion function in Eq. (1), the encoder identifies and transmits the latent variable V , which is then combined with the side information to reconstruct the original image. This is the approach followed by Ayzik and Avidan [2020]. We instead use the Wyner common information W at the decoder to reconstruct the image together with the information received from the encoder. In general, we have $R_{X|Y}^{WZ}(d) \geq R_{X|W}^{WZ}(d)$; that is, it is more beneficial to have W as side information at the decoder, as it is ‘closer’ to X in distribution. Of course, we cannot in general generate W reliably based on Y , but we argue that even an approximate reconstruction of W allows the decoder to extract only the most relevant parts of the side information in estimating X and helps the DNN that combines the

description from the encoder with the side information. In a way, we divide the post-processing into two steps: in the first step, we extract the most relevant features of the side information, and then combine these with the features provided by the encoder. Our experimental results confirms that the proposed approach helps in improving the reconstructed image quality.

We add that, the above claim would hold for any W for which $X - W - Y$ form a Markov chain. On the other hand, we particularly choose Wyner common information that minimizes $I(X, Y; W)$ as it would provide a more succinct representation with potentially better generalization performance (Ryu et al. [2020]).

3.1 Variational approach to compression with side information

In particular, the encoder learns the distribution of a latent variable \mathbf{v}_x , which is quantized and transmitted to the decoder. The decoder reconstructs the image using the quantized version of \mathbf{v}_x and \mathbf{w} . The decoder learns not only \mathbf{w} but also \mathbf{v}_y , which together allow the reconstruction of the side information \mathbf{y} . Here, the variables \mathbf{v}_x and \mathbf{v}_y capture those aspects of \mathbf{x} and \mathbf{y} that are not captured by the common variable \mathbf{w} . The graphical model for the variables introduced is shown in Fig. 2. The joint distribution of the random variables in this model is given by

$$p(\mathbf{x}, \mathbf{y}, \mathbf{w}, \mathbf{v}_x, \mathbf{v}_y) = p(\mathbf{w})p(\mathbf{v}_x)p(\mathbf{v}_y)p_\theta(\mathbf{x} | \mathbf{w}, \mathbf{v}_x; \theta_x)p_\theta(\mathbf{y} | \mathbf{w}, \mathbf{v}_y; \theta_y), \quad (6)$$

parameterized by θ_x and θ_y . To obtain tractable inference of latent variables, we introduce the following factored variational approximation of the posterior distribution:

$$q_\phi(\mathbf{w}, \mathbf{v}_x, \mathbf{v}_y | \mathbf{x}, \mathbf{y}) = q_\phi(\mathbf{v}_x | \mathbf{x}; \phi_x)q_\phi(\mathbf{w} | \mathbf{y}; \phi_w)q_\phi(\mathbf{v}_y | \mathbf{y}; \phi_y), \quad (7)$$

each of which is parameterized by a distinct DNN. See Fig. 3 for the architecture of the distributed source encoder/decoder pair that we consider. The distribution $q_\phi(\mathbf{v}_x | \mathbf{x}; \phi_x)$ is learnt by an analysis transform \mathbf{g}_{ax} at the encoder, and $q_\phi(\mathbf{v}_y | \mathbf{y}; \phi_y)$ is learnt by an analysis transform \mathbf{g}_{ay} at the decoder. The encoder maps the image \mathbf{x} to a latent representation \mathbf{v}_x by applying the transform \mathbf{g}_{ax} to it. The decoder extracts the common information $\mathbf{w} = \mathbf{f}(\mathbf{y}; \phi_f)$ between the images \mathbf{x} and \mathbf{y} by applying the transform \mathbf{f} , where ϕ_f refers to the weights of the DNN. The transform \mathbf{f} learns the marginal distribution $q_\phi(\mathbf{w} | \mathbf{y}; \phi_f)$. The decoder concatenates \mathbf{w} to the received latent variable \mathbf{v}_x , and reconstructs an estimate $\hat{\mathbf{x}} = \mathbf{g}_{sx}(\hat{\mathbf{v}}_x, \mathbf{w}; \theta_x)$ of the image \mathbf{x} by applying a synthesis transform \mathbf{g}_{sx} , which corresponds to the marginal decoder $p_\theta(\mathbf{x} | \mathbf{v}_x, \mathbf{w}; \theta_x)$. Simultaneously, the decoder learns to reconstruct the correlated image \mathbf{y} by first mapping it to the latent representation \mathbf{v}_y using an analysis transform \mathbf{g}_{ay} , and then reconstructing an estimate $\hat{\mathbf{y}} = \mathbf{g}_{sy}(\mathbf{v}_y, \mathbf{w}; \theta_y)$ by concatenating the common variable \mathbf{w} to \mathbf{v}_y and applying a synthesis transform \mathbf{g}_{sy} to it. Note that the latent representation \mathbf{v}_y is neither quantized nor perturbed with uniform noise. This is because the encoding and decoding of image \mathbf{y} happen inside the decoder without having to transmit it over a channel.

The common information \mathbf{w} is modeled using a univariate non-parametric, fully factorized density function, similarly to the latent representation \mathbf{v}_x , but without the convolution with the uniform distribution, since the common information is not required to be quantized:

$$p(\mathbf{w}) = \prod_i p_{w(i) | \psi_w^{(i)}}(w(i) | \psi_w^{(i)}), \quad (8)$$

where the vectors $\psi_w^{(i)}$ encapsulate the parameters of each univariate distribution $p_{w(i) | \psi_w^{(i)}}$. Employing the method of variational inference, we minimize the expectation of the Kullback-Liebler (KL) divergence between the approximate variational density $q_\phi(\tilde{\mathbf{v}}_x, \mathbf{v}_y, \mathbf{w} | \mathbf{x}, \mathbf{y})$ and the true posterior distribution $p(\tilde{\mathbf{v}}_x, \mathbf{v}_y, \mathbf{w} | \mathbf{x}, \mathbf{y})$ over the data distribution $p(\mathbf{x}, \mathbf{y})$:

$$\begin{aligned} & \mathbb{E}_{\mathbf{x}, \mathbf{y} \sim p(\mathbf{x}, \mathbf{y})} D_{\text{KL}} [q_\phi(\tilde{\mathbf{v}}_x, \mathbf{v}_y, \mathbf{w} | \mathbf{x}, \mathbf{y}) || p(\tilde{\mathbf{v}}_x, \mathbf{v}_y, \mathbf{w} | \mathbf{x}, \mathbf{y})] \\ &= \mathbb{E}_{\mathbf{x}, \mathbf{y} \sim p(\mathbf{x}, \mathbf{y})} \mathbb{E}_{\tilde{\mathbf{v}}_x, \mathbf{v}_y, \mathbf{w} \sim q_\phi} \left(\left(\log q_\phi(\tilde{\mathbf{v}}_x | \mathbf{x}; \phi_x) + \log q_\phi(\mathbf{v}_y | \mathbf{y}; \phi_y) + \log q_\phi(\mathbf{w} | \mathbf{y}; \phi_f) \right) \right. \\ & \quad \left. - \left(\underbrace{\log p_\theta(\mathbf{x} | \mathbf{w}, \tilde{\mathbf{v}}_x; \theta_x)}_{D_x} + \underbrace{\log p_\theta(\mathbf{y} | \mathbf{w}, \mathbf{v}_y; \theta_y)}_{D_y} + \underbrace{\log p(\mathbf{w})}_{R_w} + \underbrace{\log p(\tilde{\mathbf{v}}_x)}_{R_x} + \underbrace{\log p(\mathbf{v}_y)}_{R_y} \right) \right) + \text{const}, \end{aligned} \quad (9)$$

where the first term $q_\phi(\tilde{\mathbf{v}}_x | \mathbf{x}; \phi_x)$ is a constant because the uniform distribution has a constant width, and the second and third terms are zero because the inference model is deterministic for the

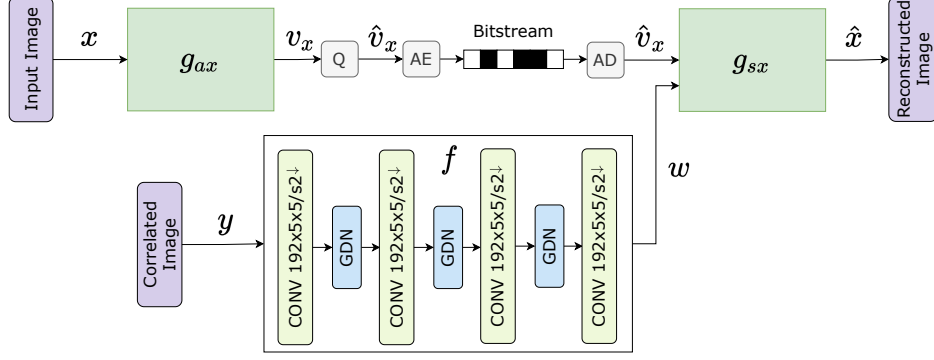


Figure 7: The proposed network architecture for distributed source coding. Block Q corresponds to a uniform quantizer, while blocks AE and AD correspond to arithmetic encoder and arithmetic decoder, respectively. Block \mathbf{f} corresponds to the transform that extracts the common information \mathbf{w} from the correlated side information image, which is concatenated with the received quantized latent vector $\hat{\mathbf{v}}_x$, and passed through the decoder \mathbf{g}_{sx} .

common information and the latent representation of the correlated image, which implies that the associated conditional entropies are zero. The terms D_x and D_y correspond to weighted distortion terms for the reconstruction of the input image and the correlated image respectively. The terms R_w , R_x and R_y correspond to the rate terms for the common information, the latent representation of the input image, and the correlated image respectively. Similarly to Eq. (5), we write the loss function with weighted terms for training the DNN:

$$L(\mathbf{g}_{ax}, \mathbf{g}_{sx}, \mathbf{g}_{ay}, \mathbf{g}_{sy}, \mathbf{f}) = (R_x + \lambda D_x) + \alpha (R_y + \lambda D_y) + \beta R_w, \quad (10)$$

where, for simplicity, we use the same weights for the distortion terms. The hyperparameter α determines how much importance is given to the reconstruction of the correlated image, and β provides a handle on the amount of common information extracted from the side information by the decoder.

We also extend the above model to use scale hyperpriors by using the model of Ballé et al. [2018] as the baseline. The details of the model are provided in the supplementary material.

4 Experiments

To compare the compression performance of our proposed model with the state of the art, we conducted a number of experiments using the PyTorch framework. Our code is publicly available¹.

Experimental setup: Fig. 7 illustrates the proposed DNN architecture for distributed source coding in detail. The transforms \mathbf{g}_{ax} and \mathbf{g}_{sx} have the same structure as those in Ballé et al. [2017]. These transforms are composed of convolutional layers, and linear (i.e., rectified linear unit) and nonlinear functions (i.e., generalized divisive normalization [GDN] and inverse generalized divisive normalization [IGDN]), which have been shown to be particularly suitable for density modelling in image compression (Ballé et al. [2017]). Note that, we have omitted the section of the network that the decoder uses to reconstruct the correlated image during training in Fig. 7. We introduce the transform \mathbf{f} as mentioned in Section 3. More details of the architecture are included in the Appendix. We constructed our dataset from the KITTI Stereo 2012 (Geiger et al. [2012]), consisting of 1578 stereo image pairs (i.e., a pair of two images taken simultaneously by different cameras), and KITTI Stereo 2015 (Menze et al. [2015, 2018]), consisting of 789 scenes with 21 stereo pairs per scene taken sequentially. It is designed to illustrate the calibrated and synchronized camera array use case. We trained every model on 1576 image pairs, and we validated and tested every model on 790 image pairs from KITTI Stereo.

Evaluation: We evaluate our models using both the multi-scale structural similarity index measure (MS-SSIM), as well as the peak SNR (PSNR) based on the mean-squared error (MSE) distortion.

¹Our code is available at: <https://github.com/ipc-lab/DWSIC>

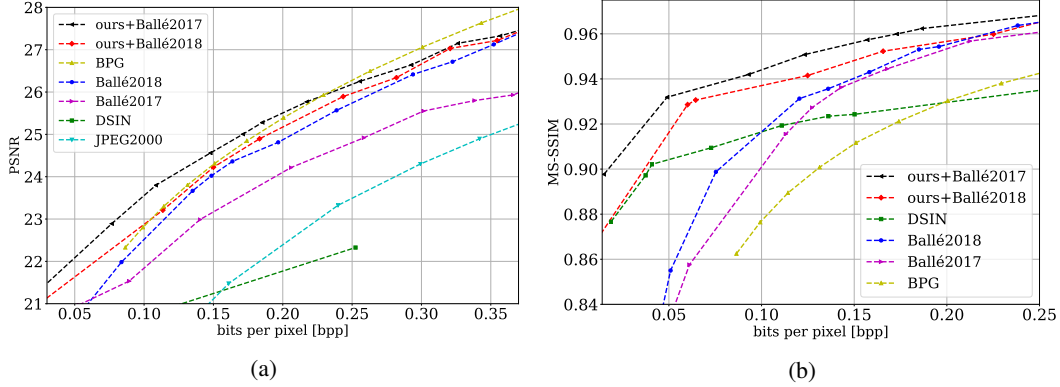


Figure 8: Comparison of different models in terms of MSE and MS-SSIM metrics. “ours + Ballé2017” refers to our proposed model with the Ballé et al. [2017] model as the baseline. Similarly, “ours + Ballé2018” has the Ballé et al. [2018] model as the baseline. “DSIN” refers to Ayzik and Avidan [2020].

The MS-SSIM has been widely reported to provide a better measure of human perception of distortion than other measures (Wang et al. [2003]).

Training: We center-crop each 375×1242 image of the KITTI Stereo dataset to obtain a 370×740 image, and then downsample it to a 128×256 image. We train the baseline model with different values of λ to obtain points for different bit rates, according to the training details in Ballé et al. [2017], using the PSNR and MS-SSIM reconstruction loss. We then train the proposed model for 500K iterations, using randomly initialized network weights. Similarly to Ballé et al. [2017], we train our models using AMSGrad optimizer Reddi et al. [2018], with a learning rate of 1×10^{-4} . The learning rate is reduced by a factor of 10 whenever the decrease in the loss function stagnates, where the lower bound on the learning rate is set to $1 \cdot 10^{-7}$. We use a batch size of 1 because of the small size of the KITTI Stereo dataset under consideration. We tested our models on 790 images from KITTI Stereo. We train the model proposed in (Ayzik and Avidan [2020]) by using the provided code². We highlight that our results for DSIN differ from the results reported in Ayzik and Avidan [2020] because we use smaller images in our experiments.

Experimental results: In this section, we discuss the performance of the proposed model and compare it with other schemes discussed in Section 1.1. Following Rippel and Bourdev [2017], we employ 4:4:4 chroma format for BPG. In Fig. 8a, we present the comparison in terms of the average PSNR. We observe an improved performance of the proposed model at low bit rates. Note that DSIN does not perform well when optimized for MSE. We observe an even more stark improvement in performance when optimized with respect to MS-SSIM in Fig. 8b, where the models that do not use side information experience a sharp drop in performance at very low bit rates, while DSIN and our proposed models, that use side information, experience a more graceful degradation of performance with decreasing bit rates. This illustrates the fact that the presence of side information is particularly useful at low bit rates, where very limited information allows reasonable reconstruction by exploiting the side information. Interestingly, even though the model by Ballé et al. [2018] performs better than the model by Ballé et al. [2017] due to the scale hyperpriors, the proposed model with the Ballé et al. [2017] model as the baseline performs better than the proposed model with the Ballé et al. [2018] model as the baseline at low bit rates. We suggest that this is due to the extra bits required to send the hyperpriors to the decoder in the Ballé et al. [2018] model, which becomes significant in the low bit rate regime we are studying.

We also present a visual comparison of the performance of the models proposed in Ballé et al. [2018], Ayzik and Avidan [2020] (referred to as DSIN), and proposed models in Fig. 12. Notice that the model by Ballé et al. [2018] fails to capture the colours at very low bit rates, as illustrated in Fig. 9b, unlike DSIN and ours. Moreover, our model successfully captures the textures and details of colours and objects in the background, while DSIN has a blurring effect on the image. This is because the DSIN model operates by first reconstructing the image based on the compressed descrip-

²<https://github.com/ayziksha/DSIN>

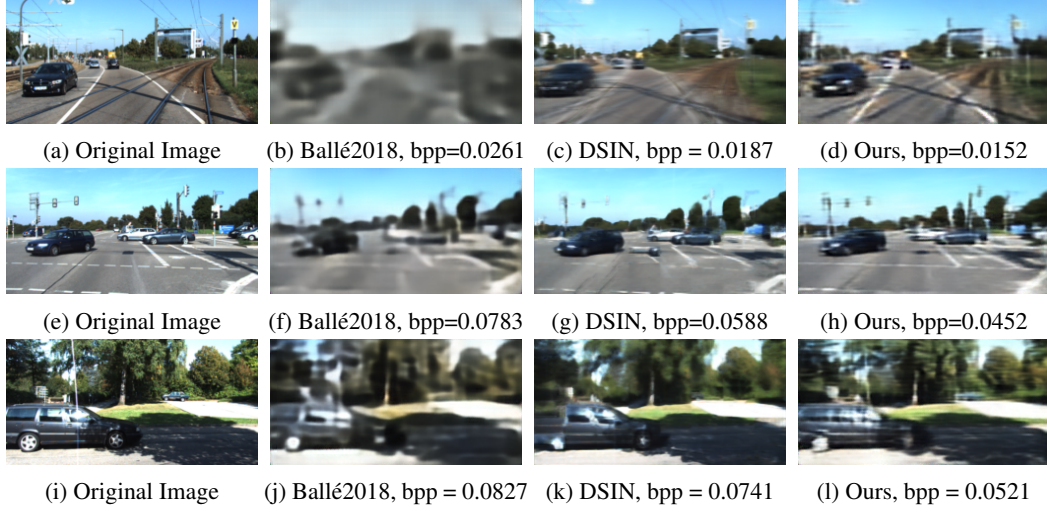


Figure 9: Visual comparison of different models trained for the MS-SSIM metric. “Ours” in the figures above refer to the “Ours + Ballé2017” model. Row 1: Compare the car, white lines in the middle and side of the road (duplication in DSIN), the tram tracks (duplication in DSIN). Row 2: compare the white lines and shadows on the road, traffic lights in the background, and the foreign object introduced by DSIN (absent in ours) next to the car. Row 3: Compare the back of the car (a missing window in DSIN reconstruction), and the details of the background (trunks of the trees, texture of trees, car in the background).

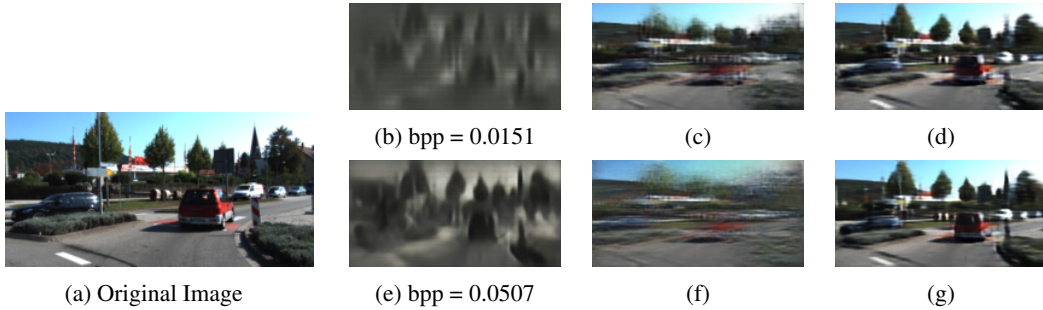
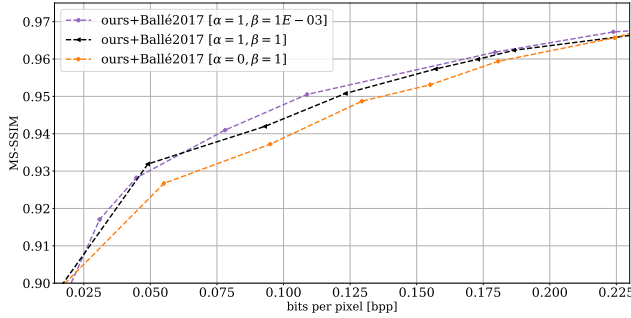


Figure 10: Images 10b and 10e: private information; images 10c and 10f: common information; images 10d and 10g: reconstructed image at the corresponding bpp values.

tion provided by the encoder, then finding the offset of corresponding patches in the intermediate reconstructions of the input and correlated images when passed through their baseline autoencoder, and then using the corresponding patches from the original side information image to refine patches in the intermediate reconstruction of the input image. If the intermediate reconstructions are not of a high quality to begin with, it can cause the wrong patches to be recognized as the corresponding, correlated patches between the input image and side information. This can cause distortions in the reconstructed image like the introduction of foreign artifacts that are not present in the original image, as shown in Fig. 12. Our model operates instead by overlaying the structural details sent by the encoder over the texture details extracted from the side information. This is illustrated in Fig. 10. We generate the visualizations of the private and common information by passing them individually through the decoder while setting the other to zero. It is observed that the common information captures the colors and texture information, which explains why our model is able to capture them at very low bit rates. It is also noted by Ayzik and Avidan [2020] that using side information helps to capture the colors at lower bit rates. We also note in Fig. 10b and 10e that as the bit rate is increased, the encoder is allowed to send more structural information; and therefore, the decoder tends to extract less definite structural details and more global color and texture details from the side information.



(a) $\alpha = 1, \beta = 1$,
bpp = 0.1239



(b) $\alpha = 1, \beta = 10^{-3}$,
bpp = 0.1101

Figure 11: Ablation study. Note the windows of the grey car in image (b) compared to the windows in image (a).

Ablation study: To study the impact of each component of the proposed model on the overall performance, we carry out an ablation study on the architecture of the decoder by varying the parameters α and β in Eq. (10), and compare the performances in Fig. 11. The default model consists of $\alpha = \beta = 1$. By setting $\alpha = 0$, we remove the part of the decoder which reconstructs the side information. We observe that in the bit rate regime under consideration, setting $\alpha = 0$ performs slightly worse than the default model. By making the value of β small, we allow the decoder to extract more common information from the side information, which is observed to provide an improvement over the default setting, particularly in the region between bpp=0.08 and bpp=0.12 for the value of β used. This suggests that β can be tuned to maximize the model’s performance at different bit rates.

5 Conclusions

We presented a novel autoencoder for lossy image compression with decoder side information exploiting the Wyner common information between the image to be reconstructed and the side information. The encoder learns to send only input image specific information, like the structural details, to the decoder, while common information, like texture and colors, are extracted by the decoder from the side information. We show that this approach allows good quality image reconstruction even at very low bit rates, improving significantly over both single image compression models, as well as previous work on image compression with side information. The loss function in Eq. (10) also provides a framework to extend this work to a setting where there are two distributed encoders having correlated images.

References

- A. Aaron, S. Rane, R. Zhang, and B. Girod. Wyner-ziv coding for video: applications to compression and error resilience. In *Data Compression Conf.*, pages 93–102, 2003.
- S. Ayzik and S. Avidan. Deep image compression using decoder side information. In *European Conf. on Computer Vision - ECCV*, pages 699–714, 2020.
- J. Ballé, V. Laparra, and E. P. Simoncelli. End-to-end optimized image compression. In *Int’l Conf on Learning Representations (ICLR)*, Toulon, France, April 2017.
- J. Ballé, D. Minnen, S. Singh, S. J. Hwang, and N. Johnston. Variational image compression with a scale hyperprior. In *International Conference on Learning Representations*, 2018.
- F. Bellard. Bpg image format. <https://bellard.org/bpg/>. 2014.
- A. Geiger, P. Lenz, and R. Urtasun. Are we ready for autonomous driving? the kitti vision benchmark suite. In *Conference on Computer Vision and Pattern Recognition (CVPR)*, 2012.

- V. K. Goyal. Theoretical foundations of transform coding. *IEEE Signal Proc. Magazine*, 18(5): 9–21, 2001.
- J. Lee, S. Cho, and S.K. Beack. Context-adaptive entropy model for end-to-end optimized image compression. In *International Conference on Learning Representations*, 2019.
- J. Liu, S. Wang, and R. Urtasun. Dsic: Deep stereo image compression. In *Proceedings of the IEEE/CVF International Conference on Computer Vision (ICCV)*, October 2019.
- F. Mentzer, E. Agustsson, M. Tschannen, R. Timofte, and L. V. Gool. Conditional probability models for deep image compression. In *IEEE/CVF Conf. on Computer Vision and Pattern Recog.*, pages 4394–4402, 2018.
- M. Menze, C. Heipke, and A. Geiger. Joint 3d estimation of vehicles and scene flow. In *ISPRS Workshop on Image Sequence Analysis (ISA)*, 2015.
- M. Menze, C. Heipke, and A. Geiger. Object scene flow. *ISPRS Journal of Photogrammetry and Remote Sensing (JPRS)*, 2018.
- D. Minnen, J. Ballé, and G. D. Toderici. Joint autoregressive and hierarchical priors for learned image compression. In *Advances in Neural Information Processing Systems*, volume 31, 2018.
- Y. Patel, S. Appalaraju, and R. Manmatha. Saliency driven perceptual image compression. In *Proc. of the IEEE/CVF Winter Conf. on App. of Computer Vision*, pages 227–236, 2021.
- S. J. Reddi, S. Kale, and S. Kumar. On the convergence of adam and beyond. In *International Conference on Learning Representations*, 2018.
- O. Rippel and L. Bourdev. Real-time adaptive image compression. In *Proceedings of the International Conference on Machine Learning*, pages 2922–2930, 2017.
- J. J. Ryu, Y. Choi, Y. H. Kim, M. El-Khamy, and J. Lee. Wyner VAE: A variational autoencoder with succinct common representation learning, 2020.
- A. Skodras, C. Christopoulos, and T. Ebrahimi. The jpeg 2000 still image compression standard. *IEEE Signal Processing Magazine*, 18(5):36–58, 2001.
- D. Slepian and J. Wolf. Noiseless coding of correlated information sources. *IEEE Transactions on Information Theory*, 19(4):471–480, 1973.
- L. Theis, W. Shi, A. Cunningham, and F. Huszár. Lossy image compression with compressive autoencoders. *arXiv preprint arXiv:1703.00395*, 2017.
- G. Toderici, D. Vincent, N. Johnston, S. J. Hwang, D. Minnen, J. Shor, and M. Covell. Full resolution image compression with recurrent neural networks. In *2017 IEEE Conference on Computer Vision and Pattern Recognition (CVPR)*, pages 5435–5443, 2017.
- W. Wang, H. Lee, and K. Livescu. Deep variational canonical correlation analysis. *ArXiv*, abs/1610.03454, 2016.
- Z. Wang, E. Simoncelli, and A. Bovik. Multiscale structural similarity for image quality assessment. In *Asilomar Conf. on Signals, Systems and Computers*, volume 2, pages 1398 – 1402, 2003.
- A. Wyner. The common information of two dependent random variables. *IEEE Transactions on Information Theory*, 21(2):163–179, 1975.
- A. Wyner and J. Ziv. The rate-distortion function for source coding with side information at the decoder. *IEEE Transactions on Information Theory*, 22(1):1–10, 1976.

6 Appendix

6.1 Implementation details - Ballé et al. [2017] baseline

Training each model took around ~ 36 hours per model, i.e., obtaining one point on the curves plotted in Fig. 8a and 8b. As shown in Fig. 7, our model consists of three main blocks \mathbf{g}_{ax} for encoding the input image to a latent vector, \mathbf{f} for extracting the common information \mathbf{w} from the side information, and \mathbf{g}_{sx} for decoding the concatenation of common information and the quantized latent vector to the reconstructed image. In Table 1 and 2, a top-down architecture of each block is provided. Convolution layer parameters are denoted as: number of filter \times kernel height \times kernel width / sampling stride, where \uparrow and \downarrow indicate upsampling and downsampling, respectively. GDN (IGDN) corresponds to (inverse) generalized divisive normalization operation described in Ballé et al. [2017].

Table 1: Network architecture for \mathbf{g}_{ax} and \mathbf{f} blocks.

Layers
Conv2D ($192 \times 5 \times 5 / 2 \downarrow$)
GDN
Conv2D ($192 \times 5 \times 5 / 2 \downarrow$)
GDN
Conv2D ($192 \times 5 \times 5 / 2 \downarrow$)
GDN
Conv2D ($192 \times 5 \times 5 / 2 \downarrow$)

Table 2: Network architecture for \mathbf{g}_{sx} block.

Layers
Conv2D ($192 \times 5 \times 5 / 2 \uparrow$)
IGDN
Conv2D ($192 \times 5 \times 5 / 2 \uparrow$)
IGDN
Conv2D ($192 \times 5 \times 5 / 2 \uparrow$)
IGDN
Conv2D ($3 \times 5 \times 5 / 2 \uparrow$)

During training, to simulate quantization of the latent representation and to compute the likelihoods of the latent representation, an entropy bottleneck block is used, which corresponds to the univariate non-parametric density model used for modeling the distribution of the latent representation. The entropy bottleneck block implementation is similar to the one provided in Ballé et al. [2018]. The entropy bottleneck block is also used to estimate the likelihoods of the common variable \mathbf{w} .

During training, the side information image \mathbf{y} is also passed through the autoencoder, where it is first mapped to its latent representation using the encoder block \mathbf{g}_{ay} , which has the same structure as \mathbf{g}_{ax} , and then reconstructing \mathbf{y} by passing its latent representation through the decoder block \mathbf{g}_{sy} , which has the same structure as \mathbf{g}_{sx} . Note that the latent representation of \mathbf{y} is not quantized.

Note that we opt for sliding Gaussian window of size 7×7 , instead of the popular choice of 11×11 , for MS-SSIM reconstruction loss function calculations due to having utilised image size of 128×256 in our training setup.

6.2 Wyner-Ziv rate-distortion function with Wyner common information

Let W denote the Wyner common information between source X and side information Y , where $X-W-Y$ form a Markov chain. It is clear that the rate-distortion function would reduce if we provide W as additional side information to the receiver, i.e., we have $R_{X|Y}^{WZ}(d) \geq R_{X|YW}^{WZ}(d)$, $\forall d \geq 0$. On the other hand, note that, $R_{X|YW}^{WZ}(d) = \inf I(X; V | W, Y)$, over all V for which $V-X-W-Y$ form a Markov chain, and there exist a function f that satisfies $\mathbb{E}[D(X, f(V, W, Y))] \leq d$. Since, $I(X; V | W, Y) = I(X; V | W)$, and conditioned on W, Y does not help in the estimation of X . Hence, we conclude that $R_{X|Y}^{WZ}(d) \geq R_{X|YW}^{WZ}(d) = R_{X|W}^{WZ}(d)$.

6.3 Derivation of the variational loss function in Eq. (9)

We have

$$\begin{aligned} & \mathbb{E}_{\mathbf{x}, \mathbf{y} \sim p(\mathbf{x}, \mathbf{y})} D_{\text{KL}} \left[q_{\phi}(\tilde{\mathbf{v}}_x, \mathbf{v}_y, \mathbf{w} \mid \mathbf{x}, \mathbf{y}) \parallel p(\tilde{\mathbf{v}}_x, \mathbf{v}_y, \mathbf{w} \mid \mathbf{x}, \mathbf{y}) \right] \\ &= \mathbb{E}_{\mathbf{x}, \mathbf{y} \sim p(\mathbf{x}, \mathbf{y})} \mathbb{E}_{\tilde{\mathbf{v}}_x, \mathbf{v}_y, \mathbf{w} \sim q_{\phi}} \left[\log \left(\frac{q_{\phi}(\tilde{\mathbf{v}}_x, \mathbf{v}_y, \mathbf{w} \mid \mathbf{x}, \mathbf{y})}{p(\tilde{\mathbf{v}}_x, \mathbf{v}_y, \mathbf{w} \mid \mathbf{x}, \mathbf{y})} \right) \right] \end{aligned} \quad (11)$$

$$= \mathbb{E}_{\mathbf{x}, \mathbf{y} \sim p(\mathbf{x}, \mathbf{y})} \mathbb{E}_{\tilde{\mathbf{v}}_x, \mathbf{v}_y, \mathbf{w} \sim q_{\phi}} \left[\log \left(\frac{q_{\phi}(\tilde{\mathbf{v}}_x, \mathbf{v}_y, \mathbf{w} \mid \mathbf{x}, \mathbf{y}) p(\mathbf{x}, \mathbf{y})}{p(\tilde{\mathbf{v}}_x, \mathbf{v}_y, \mathbf{w}, \mathbf{x}, \mathbf{y})} \right) \right] \quad (12)$$

$$= \mathbb{E}_{\mathbf{x}, \mathbf{y} \sim p(\mathbf{x}, \mathbf{y})} \mathbb{E}_{\tilde{\mathbf{v}}_x, \mathbf{v}_y, \mathbf{w} \sim q_{\phi}} \left[\log \left(\frac{q_{\phi}(\tilde{\mathbf{v}}_x \mid \mathbf{x}; \phi_x) q_{\phi}(\mathbf{v}_y \mid \mathbf{y}; \phi_y) q_{\phi}(\mathbf{w} \mid \mathbf{y}; \phi_f) p(\mathbf{x}, \mathbf{y})}{p(\mathbf{x} \mid \tilde{\mathbf{v}}_x, \mathbf{w}; \theta_x) p(\mathbf{y} \mid \mathbf{v}_y, \mathbf{w}; \theta_y) p(\mathbf{w}) p(\tilde{\mathbf{v}}_x) p(\mathbf{v}_y)} \right) \right] \quad (13)$$

$$\begin{aligned} &= \mathbb{E}_{\mathbf{x}, \mathbf{y} \sim p(\mathbf{x}, \mathbf{y})} \mathbb{E}_{\tilde{\mathbf{v}}_x, \mathbf{v}_y, \mathbf{w} \sim q_{\phi}} \left(\left(\log q_{\phi}(\tilde{\mathbf{v}}_x \mid \mathbf{x}; \phi_x) + \log q_{\phi}(\mathbf{v}_y \mid \mathbf{y}; \phi_y) + \log q_{\phi}(\mathbf{w} \mid \mathbf{y}; \phi_f) \right) \right. \\ &\quad \left. - \left(\underbrace{\log p_{\theta}(\mathbf{x} \mid \mathbf{w}, \tilde{\mathbf{v}}_x; \theta_x)}_{D_x} + \underbrace{\log p_{\theta}(\mathbf{y} \mid \mathbf{w}, \mathbf{v}_y; \theta_y)}_{D_y} + \underbrace{\log p(\mathbf{w})}_{R_w} + \underbrace{\log p(\tilde{\mathbf{v}}_x)}_{R_x} + \underbrace{\log p(\mathbf{v}_y)}_{R_y} \right) \right) + \text{const}, \end{aligned} \quad (14)$$

where Eq. (13) follows from Eq. (6) and (7).

6.4 Hyperprior-based model extension

We extend the proposed model to include the hyperpriors \mathbf{z}_x and \mathbf{z}_y , similarly to Ballé et al. [2018], by stacking the parametric transforms \mathbf{h}_{ax} and \mathbf{h}_{ay} on top of \mathbf{v}_x and \mathbf{v}_y , respectively, such that $\mathbf{z}_x = \mathbf{h}_{ax}(\mathbf{v}_x; \phi_{hx})$ and $\mathbf{z}_y = \mathbf{h}_{ay}(\mathbf{v}_y; \phi_{hy})$. The hyperprior models the spatial dependencies between the elements of the latent variable, and enables better compression by the entropy coder. Conditioned on the hyperprior variable, each element of \mathbf{v}_x , denoted by $v_x(i)$, $i = 1, \dots, m$, is assumed to be an independent zero-mean Gaussian with its own standard deviation σ_i , where the standard deviations are predicted by applying a parametric transform \mathbf{h}_{sx} to the hyperprior $\tilde{\mathbf{z}}_x$, such that $\sigma_x = \mathbf{h}_{sx}(\tilde{\mathbf{z}}_x; \theta_{hx})$. A similar process is followed for the hyperpriors \mathbf{z}_y .

Similarly to Ballé et al. [2018], the quantization of the hyperprior is replaced by perturbing it with uniform random noise during training to obtain $\tilde{\mathbf{z}}_x$. The joint density of $\tilde{\mathbf{v}}_x$ and $\tilde{\mathbf{z}}_x$ through the inference mechanism is modeled as:

$$q_{\phi}(\tilde{\mathbf{v}}_x, \tilde{\mathbf{z}}_x \mid \mathbf{x}; \phi_x, \phi_{hx}) = \prod_i \mathcal{U} \left(\tilde{v}_x(i) \mid v_x(i) - \frac{1}{2}, v_x(i) + \frac{1}{2} \right) \cdot \prod_j \mathcal{U} \left(\tilde{z}_x(j) \mid z_x(j) - \frac{1}{2}, z_x(j) + \frac{1}{2} \right). \quad (15)$$

The prior of $\tilde{\mathbf{v}}_x$, conditioned on the perturbed hyperprior $\tilde{\mathbf{z}}_x$, is given by:

$$p_{\theta}(\tilde{\mathbf{v}}_x \mid \tilde{\mathbf{z}}_x; \theta_{hx}) = \prod_i \left(\mathcal{N}(0, \tilde{\sigma}_i^2) * \mathcal{U}(-0.5, 0.5) \right) (\tilde{v}_x(i)) \quad (16)$$

$$\text{with } \tilde{\sigma}_i = \mathbf{h}_{sx}(\tilde{\mathbf{z}}_x; \theta_{hx}), \quad (17)$$

where θ_{hx} refers to the weight of the neurons, and $\mathcal{N}(\cdot, \cdot)$ and $\mathcal{U}(\cdot, \cdot)$ correspond to the normal distribution and the uniform distribution on $\tilde{v}_x(i)$. As we assume no prior beliefs about the hyperpriors, the probability density of the perturbed hyperpriors $\tilde{\mathbf{z}}_x$ is modeled using a univariate non-parametric, fully factorized density model (Ballé et al. [2018])

$$p(\tilde{\mathbf{z}}_x) = \prod_i \left(p_{z_x(i) \mid \psi^{(i)}}(\psi^{(i)} * \mathcal{U}(-0.5, 0.5))(\tilde{z}_x(i)), \right) \quad (18)$$

where the vectors $\psi^{(i)}$ encapsulate the parameters of each univariate distribution $p_{z_x(i) \mid \psi^{(i)}}$. During evaluation, the quantized latent representation $\tilde{\mathbf{v}}_x$ and the quantized hyperprior $\tilde{\mathbf{z}}_x$ are encoded and

transmitted as a bit-stream by the arithmetic encoder using the Gaussian prior density model and the univariate non-parametric density model respectively.

Employing the method of variational inference, the loss function of this model works out to be

$$\begin{aligned}
& \mathbb{E}_{\mathbf{x}, \mathbf{y} \sim p(\mathbf{x}, \mathbf{y})} \text{D}_{\text{KL}} \left[q_{\phi}(\tilde{\mathbf{v}}_x, \mathbf{v}_y, \mathbf{w}, \tilde{\mathbf{z}}_x, \mathbf{z}_y \mid \mathbf{x}, \mathbf{y}) \parallel p(\tilde{\mathbf{v}}_x, \mathbf{v}_y, \mathbf{w}, \tilde{\mathbf{z}}_x, \mathbf{z}_y \mid \mathbf{x}, \mathbf{y}) \right] \quad (19) \\
& = \mathbb{E}_{\mathbf{x}, \mathbf{y} \sim p(\mathbf{x}, \mathbf{y})} \mathbb{E}_{\tilde{\mathbf{v}}_x, \mathbf{v}_y, \mathbf{w}, \tilde{\mathbf{z}}_x, \mathbf{z}_y \sim q_{\phi}} \left(\left(\log q_{\phi}(\tilde{\mathbf{v}}_x, \tilde{\mathbf{z}}_x \mid \mathbf{x}; \phi_x) + \log q_{\phi}(\mathbf{v}_y, \mathbf{z}_y \mid \mathbf{y}; \phi_y) + \log q_{\phi}(\mathbf{w} \mid \mathbf{y}; \phi_f) \right) \right. \\
& \quad \left. - \left(\log p_{\theta}(\mathbf{x} \mid \mathbf{w}, \tilde{\mathbf{v}}_x; \theta_x) + \log p_{\theta}(\mathbf{y} \mid \mathbf{w}, \mathbf{v}_y; \theta_y) + \log p(\mathbf{w}) + \log p_{\theta}(\tilde{\mathbf{v}}_x \mid \tilde{\mathbf{z}}_x; \theta_{hx}) + \log p_{\theta}(\mathbf{v}_y \mid \mathbf{z}_y; \theta_{hy}) \right. \right. \\
& \quad \quad \left. \left. + \underbrace{\log p(\tilde{\mathbf{z}}_x)}_{R_{z_x}} + \underbrace{\log p(\mathbf{z}_y)}_{R_{z_y}} \right) \right) + \text{const}, \quad (20)
\end{aligned}$$

where the term R_{z_x} corresponds to the rate of the hyperprior associated with the input image, while the term R_{z_y} corresponds to the rate of the hyperprior associated with the correlated image.

6.5 Implementation details - Ballé et al. [2018] baseline

The proposed model based on Ballé et al. [2018] includes four more additional blocks compared to the proposed model based on Ballé et al. [2017]: the parametric transforms \mathbf{h}_{ax} and \mathbf{h}_{sx} related to the hyperpriors of the input image, and the parametric transforms \mathbf{h}_{ay} and \mathbf{h}_{sy} related to the hyperpriors of the side information. \mathbf{h}_{ax} and \mathbf{h}_{ay} simply have an inverted structure with respect to \mathbf{h}_{sx} and \mathbf{h}_{sy} . In Table 3 and 4, a top-down architecture of each block is provided.

Table 3: Network architecture for \mathbf{h}_{ax} block.

Layers
Conv2D ($192 \times 3 \times 3$ / 1 ↓)
ReLU
Conv2D ($192 \times 5 \times 5$ / 2 ↓)
ReLU
Conv2D ($192 \times 5 \times 5$ / 2 ↓)

Table 4: Network architecture for \mathbf{h}_{sx} block.

Layers
Conv2D ($192 \times 5 \times 5$ / 2 ↑)
ReLU
Conv2D ($192 \times 5 \times 5$ / 2 ↑)
ReLU
Conv2D ($192 \times 3 \times 3$ / 1 ↑)

6.6 DSIN limitations

In this section, we illustrate the reason why the DSIN model causes distortions in the image reconstructions. An image Y_{syn} is assembled by the patch finder in the DSIN model by first reconstructing two intermediate images from the input image and the side information from their latent representations, and then finding the most correlated corresponding patches in the two intermediate images. From the offsets of the corresponding patches, the corresponding patches are then taken from the original side information image, and the image Y_{syn} is assembled. In Fig. 12c, we illustrate that if the intermediate reconstructions of the image and the side information are not good, the patch finder may recognize wrong patches to be the most correlated ones, thus leading to the distorted image Y_{syn} seen in the figure. This leads to an image reconstruction in which patches of the image seem to get blurred or shifted.



Figure 12: Illustration of the distortion caused by the patch finder in DSIN.

6.7 Evaluation on full-sized images

In Fig. 13 and 14, we evaluate our trained models on 375×1242 images from KITTI Stereo. It is interesting to note that although we trained our model and the DSIN model on smaller images of size 128×256 , they perform well on larger images too. We see a significant improvement in the reconstructed images by our proposed model over DSIN, especially in capturing the details of objects which are far away. This is because farther objects do not shift as much as the closer objects in stereo images, and therefore are captured much better as the common information between the stereo images.



(a) DSIN, bpp=0.0435



(b) Ours, bpp=0.0437

Figure 13: Reconstruction comparison between DSIN (top) and ours (bottom) when evaluated on full-sized images from KITTI Stereo. Compare the texture details captured on the pavement and on the white building.



(a) DSIN, bpp=0.0449



(b) Ours, bpp=0.0431

Figure 14: Reconstruction comparison between DSIN (top) and ours (bottom) when evaluated on full-sized images from KITTI Stereo. Compare the edges of the windows, the fine and texture details of the grass and the tree.

6.8 Additional visual examples

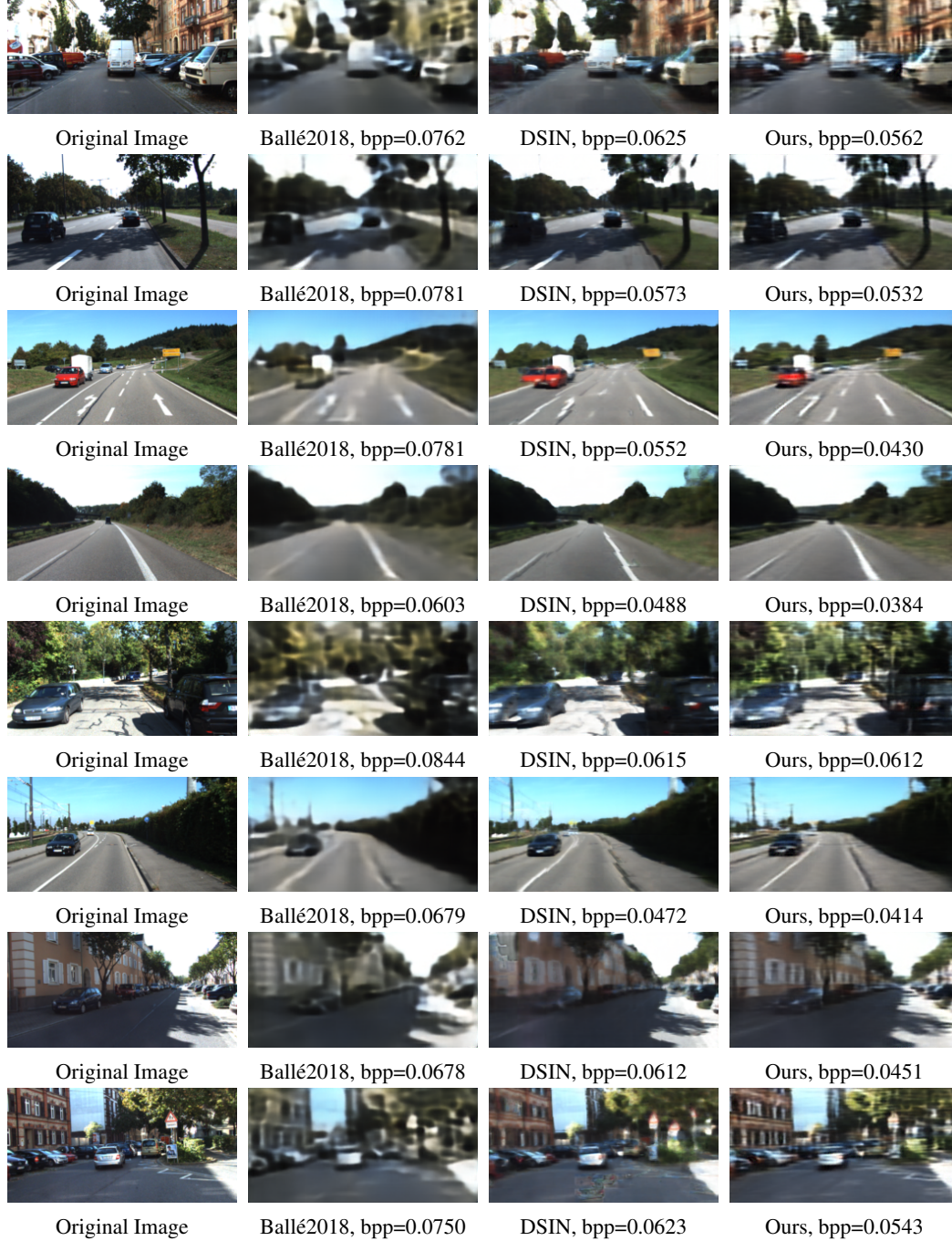


Figure 15: Additional visual comparison of different models from KITTI Stereo in a low bpp range. The models are trained using MS-SSIM distortion function. Notice that in some examples, such as rows 3, 4, and 6, the DSIN model adds some fracture-like effects to the reconstructed image.

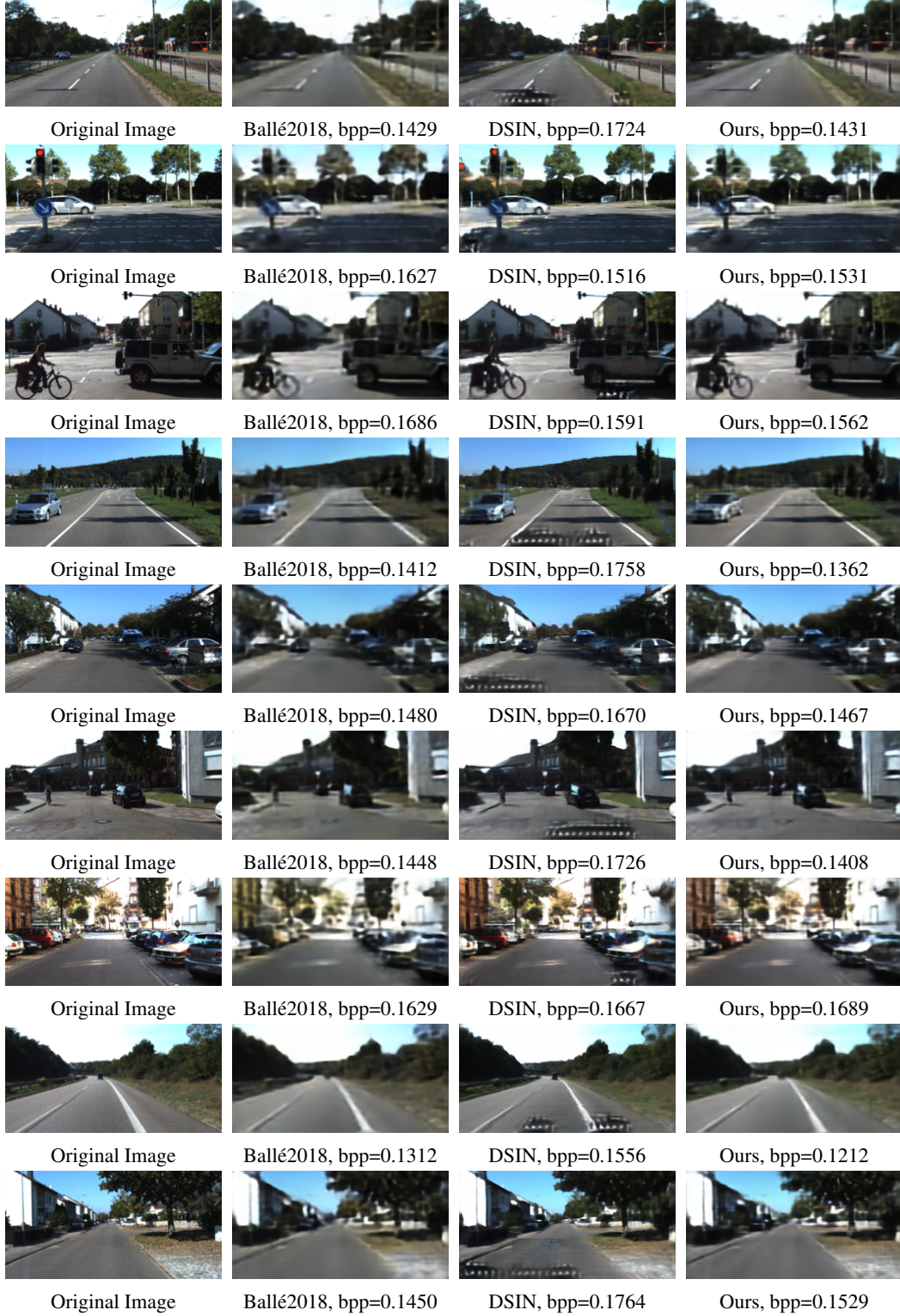


Figure 16: Additional visual comparison of different models from KITTI Stereo in a higher bpp range. The models are trained using MS-SSIM distortion function. Notice that while DSIN provides good quality reconstructions, it also introduces foreign artifacts into the images.



Figure 17: Additional visual comparison of different models from KITTI Stereo image dataset. The models are trained using the MSE distortion function. For MSE distortion, DSIN did not perform as well as the other models. Thus BPG is used for compression rather than DSIN. Compared to our model, BPG fails to provide details such as texture and edges in the reconstructed image despite having a higher bpp. Similar to DSIN, BPG also introduces some artifacts into the images. Also note that BPG method overall fails to reach the very low bit rates as seen in Fig. 8a and 8b.

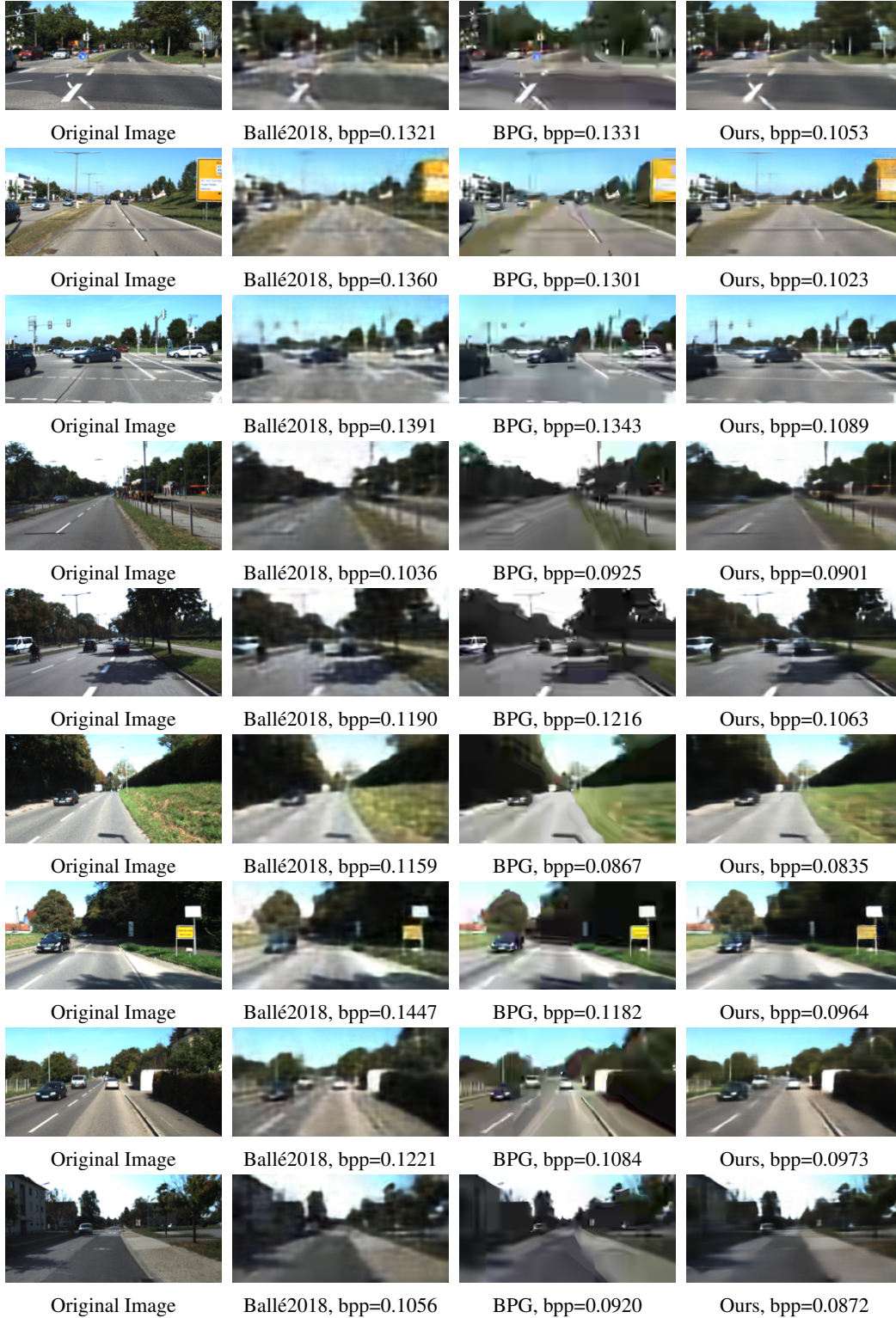


Figure 18: Additional visual comparison of different models from KITTI Stereo image dataset. The models are trained using MSE distortion function. Observe that BPG mainly achieves to restore the coarse edges but fails to capture fine features and texture details, unlike ours.